RSC Advances

Check for updates

Functional utilization of biochar derived from *Tenebrio molitor* feces for CO_2 capture and supercapacitor applications†

Saier Wang, Ying Shi, Huiming Xiang, Ru Liu, Lianghu Su, [iD] * Longjiang Zhang and Rongting Ji*

Biochar has attracted great interest in both CO_2 capture and supercapacitor applications due to its unique physicochemical properties and low cost. Fabrication of eco-friendly and cost-effective biochar from high potential biomass *Tenebrio molitor* feces can not only realize the functional application of waste, but also a potential way of future carbon capture and energy storage technology. In this study, a novel KOH activation waste-fed *Tenebrio molitor* feces biochar (TMFB) was developed and investigated in terms of CO_2 capture and electrochemical performance. When activated at 700 °C for 1 h, the specific surface area of the feces biochar (TMFB-700A) increased significantly from 232.1 to 2081.8 m^2 g^{-1}. In addition, well-developed pore distribution facilitates CO_2 capture and electrolyte diffusion. TMFB-700A can quickly adsorb a large amount of CO_2 (3.05 mol kg^{-1}) with excellent recycling performance. TMFB-700A also exhibited promising electrochemical performance (335.8 F g^{-1} at 0.5 A g^{-1}) and was used as electrode material in a symmetrical supercapacitor. It provided a high energy density of 33.97 W h kg^{-1} at a power density of 0.25 kW kg^{-1} with 90.47% capacitance retention after 10 000 charge−discharge cycles. All the results demonstrated that TMFB could be a potential bifunctional material and provided valuable new insights for *Tenebrio molitor* feces high-value utilization.

Introduction

According to the latest global assessment of climate change mitigation progress provided by the Intergovernmental Panel on Climate Change (IPCC), greenhouse gas emissions are continuing to increase world wide.[1] CO_2, the largest share of greenhouse gases (74.5%), has increased in atmospheric concentrations by about 50% from pre-industrial levels of 280 ppm.[2,3] It is the major contributor to global warming, causing irreversible damage to climate, environment, and ecosystems. The goal of keeping global warming below 2 °C or even 1.5 °C seems largely unattainable without immediate CO_2 emission reduction.[4] On the one hand, CO_2 capture technology is considered the most direct and cost-effective way to reduce CO_2 emissions in the short or medium term due to high energy utilization efficiency, small energy requirements, and simple operation.[5] On the other hand, developing energy storage technologies to reduce reliance on fossil fuel combustion is a fundamental way for CO_2 emission reduction.[6,7] With high power/energy density, long cycle life, and fast charge/discharge

rates, supercapacitors can be used as promising energy storage devices to meet the growing power demand of energy storage systems in the 21st century.[8,9]

Whether CO_2 capture or supercapacitor, the development and breakthrough of technology depends on the renewal of materials. Among new materials, biochar, as a renewable carbon source, has a large specific surface area and well-developed pore volume, which is not only beneficial to CO_2 capture but also to electrolyte diffusion.[10,11] In addition, biochar has stable physicochemical properties, good electrical conductivity, and low resistance.[12] Therefore, they can be used as both CO_2 capture materials and electrode materials for supercapacitor. Carbonaceous materials such as agricultural and forestry waste and municipal waste can be used as raw materials to prepare biochar.[13] Hence, the cost of biochar is only ~1/10 of other CO_2 capture or supercapacitor materials.[14] Moreover, the process of converting solid waste to biochar and then to applications belongs to carbon utilization, which also contributes to the reduction of greenhouse gases and reflects the circular economy.[15] Currently, there have been some studies confirmed that the CO_2 capture or supercapacitor applications performance of biochar depends on physical and chemical properties, such as specific surface area, porosity, basicity of surface, surface functional groups, presence of metals, degree of graphitization and structural defects density.[16,17] These properties of biochar are mainly affected by biomass precursor,

Nanjing Institute of Environmental Sciences, Ministry of Ecology and Environment, 8 Jiangwangmiao Street, Nanjing 210042, P. R. China. E-mail: sulianghu@126.com; jirongting@nies.org

pretreatment, pyrolysis temperature, activation and modification.[18] However, to the best of our knowledge, most of the research in biochar basically focused on a single application instead of synergistic characteristic terms of supercapacitors and CO_2 capture performance.

Tenebrio molitor was regarded by the Food and Agriculture Organization of the United Nations as a new type of high-protein edible insect and a future food source in 2003 and has attracted people's attention in recent years.[19,20] The scale of *Tenebrio molitor* breeding has been increasing yearly because of the vigorous promotion by governments of various countries.[21] *Tenebrio molitor* breeding also has environmental benefits, as agricultural waste can be used directly as feed.[19,20] *Tenebrio molitor* will convert 20–50% of the feed into feces, implying that a large number of feces will be produced in large-scale breeding.[22] Unlike other animal feces, *Tenebrio molitor* feces (TMF) have high trace element content, less water content and no peculiar smell, indicating a potential biomass resource.[23–25] TMF is often used directly as fertilizer, but its fertility is limited and may cause seedling burnt without fermentation. Compared with traditional composting and anaerobic digestion, converting TMF into biochar through pyrolysis treatment under anaerobic or oxygen-limited conditions can process a large number of feces within a period of time while providing potential materials. A highly aromatized *Tenebrio molitor* frass biochar synthesized by Yang *et al.* has a high specific surface area (238.37 m² g⁻¹) and good adsorption performance for dyes.[26,27] However, the application capacity of raw biochar is very limited and there is a lack of in-depth studies on potential TMF biochar. Various activation methods can be used further to increase the specific surface area of TMF biochar, optimize its pore structure and enhance its functionality.[28] Therefore, the development of functional TMF biochar using activation for CO_2 capture and supercapacitor is the key to the high-value utilization of TMF.

Herein, *Tenebrio molitor* was fed with fruit waste, and its feces were collected to prepare TMF biochar through pyrolysis and KOH activation. It is worth noting that the *Tenebrio molitor* feces were selected as a biomass precursor because they have low cost, extensive availability and great potential, and are rarely reported. The physical and chemical properties (specific surface area, surface functional groups, micromorphology, *etc.*) changes of the prepared TMF biochar under different activation temperature were characterized and analyzed. The CO_2 capture capacity and regeneration capacity of TMF biochar were evaluated and compared with other reported biochar. The specific capacitance, stability and energy/power density of TMF biochar were tested in three- and two-electrode systems and an attempt was made to reveal the relationship between electrochemical performance and structure. This study proposed a clean production pathway to convert TMF into functional biochar and offer valuable new insights for resource utilization of TMF.

Experimental

Biochar preparation and activation

Tenebrio molitor was cultivated at the insect-rearing laboratory in Huangshan, Anhui province, China (Fig. S1†). The laboratory was adjacent to a fruit planting base, ensuring the feed source of waste fruit for *Tenebrio molitor*. Fresh TMF were sieved through a 0.42 mm mesh size and then soaked in 1 M HCl for 12 h to remove impurities. Then, TMF were washed with deionized water until the neutrality was reached, and dried in an oven at 105.0 °C for 6 h. The TMF biochars (TMFB) were prepared *via* pyrolysis at 500.0 °C (reactor temperature) for 60 min with a heating rate of 10.0 °C min⁻¹ in a muffle furnace (HPM-2G, AS ONE Corp., Japan) under an N_2 atmosphere, with a yield of 73.8%.

For activation, the TMFB was further mixed homogeneously with KOH at a mass ratio of 1 : 4 and activated at 600.0 °C, 700.0 °C, and 800.0 °C (reactor temperature) for 1 h using a muffle furnace (HPM-2G, AS ONE Corp., Japan) under N_2. After cooling, the activated TMFB was ultrasonically cleaning to remove KOH with deionized water and dried at 105 °C for 6 h, with yields of 75.2%, 63.7%, and 46.6% at 600.0 °C, 700.0 °C, and 800.0 °C. The TMFB samples activated at 600.0 °C, 700.0 °C, and 800.0 °C were named TMFB-600A, TMFB-700A, and TMFB-800A, respectively.

Material characterization and instrument specifications

10.0 g of TMF was dispersed in 25 mL of deionized water and left for 30 minutes, the supernatant was used to test the pH. The pH values were measured using a pH meter (S470 SevenExcellence, Mettler Toledo, Switzerland). The mass (M1) and uncompacted volume (V1) of biochars were determined using an analytical balance and a graduated cylinder, and bulk density was calculated as M1/V1.[29] Metal content analysis was performed *via* inductively-coupled plasma mass spectrometry (ICP-MS, Agilent 7700, Agilent Technologies Inc., USA) after acid digestion pre-treatment. X-ray diffraction (XRD) was used to analyze the surface-phase composition of the biochar sample (D8, Bruker, Germany) using an accelerating voltage of 40.0 kV and current of 40.0 mA over a 2θ range of 5.0°–80.0°. Graphite monochromatic Cu Kα radiation was used. Fourier transform infrared spectroscopy (FT-IR) was performed in the 4000.0–400.0 cm⁻¹ range (Spectrum 200, PerkinElmer, USA) to analyze the functional groups within the samples. Raman spectra were collected using a Raman spectrophotometer (HR800, HORIBA, Japan) with 514.5 nm laser radiation in the 500.0–3000.0 cm⁻¹ range. De-baseline and integration areas of the Raman spectrum were manipulated in PeakFit software. The surface functionalities of the sample were obtained *via* X-ray photoelectron spectroscopy (XPS) using a photoelectron spectrometer (ESCALAB 250Xi, Thermo Scientific, USA) and calibrated with the C 1s peak. The XPS of materials were deconvoluted and peak-fitted in Advantage software. The morphologies of the resulting biochar samples were characterized *via* scanning electron microscopy (SEM, Regulus 8230, Hitachi, Japan) and transmission electron microscopy (TEM, Talos 120 L, ThermoScientific, USA). The adsorption/desorption isotherm of N_2 at 77.0 K was obtained using a surface area and pore size analyzer (ASAP 2460, Micrometrics, USA). The Brunauer–Emmett–Teller (BET) theory was used to calculate the total specific surface area and the Barret–Joyner–Halenda (BJH) model was used for pore size analysis.[30]

CO₂ capture measurements

The CO_2 capture capacity of the biochar sample was determined by a volumetric adsorption analyzer (ASAP 2460, Micrometrics, USA) at 25.0 °C and 0.1 MPa. Before each measurement, the sample was degassed under vacuum (10.0 μm Hg) at 150.0 °C for 12 h. The gravimetric CO_2 capture capacity of the biochars was assessed using a thermogravimetric analyzer (TGA, DSC 3+, Mettler Toledo, Switzerland). Under N_2 flowing at 80.0 mL min^{-1}, 5.0 mg of biochar sample was placed in TGA where it was heated to 120.0 °C at 5.0 °C min^{-1} for 1 h to remove pre-adsorbed gas molecules such as water vapor. The temperature was lowered to 30.0 °C under a continuous N_2 flow and the temperature was maintained for 2 h. Then, CO_2 was flowed at 50.0 mL min^{-1} for 2 h for the capture test to ensure that capture equilibrium was reached. The TGA was also used to evaluate the recyclability of the biochar. The same pretreatment and stabilization conditions used for gravimetric CO_2 capture capacity were applied to the cycling stability test. After pretreatment, 10 cycles of adsorption and desorption were performed. Each cycle consisted of adsorption for 1 h under flowing CO_2 (50.0 mL min^{-1}) followed by desorption for 1.5 h under an N_2 purge (80.0 mL min^{-1}).

Electrochemical measurement

Electrochemical performance tests of biochars were carried out using an electrochemical workstation (CHI 760E, Shanghai Chenhua Inc, China) at 25.0 °C. The main tests were cyclic voltammetry (CV), constant current charge and discharge (GCD), alternating current impedance (EIS), and cycling performance tests. The working electrode for the traditional three-electrode system was prepared as follows: 75.0 mg of the active sample and 15.0 mg of acetylene black were ground for 20 min, and then 10.0 mg of adhesive PTEF was added. The mixed sample was dissolved in isopropanol and stirred for 24 h, and the as-obtained slurry was applied to a 1.0×1.0 cm^2 region on the surface of the foamed nickel. A mass load of 2.0–4.0 mg cm^{-2} was used. The coated nickel foam was dried at 75.0 °C for 2 h and pressed into thin foil at a pressure of approximately 10.0 MPa to obtain a working electrode. A three-electrode system was constructed with platinum wire used as the counter electrode, saturated calomel as the reference electrode, and 6.0 M KOH as the electrolyte.

TMFB, TMFB-600A, TMFB-700A, and TMFB-800A were used as positive and negative electrodes during the manufacture of aqueous symmetrical supercapacitor devices. The electrochemical performance of the two-electrode electrochemical full cell was measured at 25.0 °C with 6.0 M KOH as the electrolyte.

Equations

The mathematical expression of Langmuir equation is as follows:

$$q_e = \frac{q_s K_L P_{CO_2}}{1 + K_L P_{CO_2}} \tag{1}$$

where q_s (mmol g^{-1}) represents the maximum monolayer adsorption capacity of the adsorbent, P_{CO2} (MPa) represents the equilibrium pressure of the adsorbed gas, and K_L (MPa^{-1}) represents the Langmuir adsorption constant.

The mathematical expression of Langmuir equation is as follows:

$$q_e = K_F P_{CO_2}^{1/n} \tag{2}$$

where K_F (mmol g^{-1} MPa$^{-1/n}$) represents the Freundlich isotherm constant and n represents the Freundlich coefficient.

Specific capacitances C derived from galvanostatic charge–discharge (GCD) tests can be determined using the equation:

$$C = \frac{I \times \Delta t}{m \times \Delta V} \tag{3}$$

where I represents the current density (A g^{-1}), Δt denotes the discharge time (s), m corresponds to the mass of active material (g), and ΔV is the voltage window (V).

The specific capacitance (C_{cell}, F g^{-1}), energy density (E, W h kg^{-1}) and power density (P, W kg^{-1}) of the symmetric supercapacitor device were calculated with the following equations:

$$C_{cell} = \frac{I \times \Delta t}{M \times \Delta V} \tag{4}$$

$$E = \frac{C_{cell} \times \Delta V^2}{2 \times 3.6} \tag{5}$$

$$P = \frac{E}{t} \tag{6}$$

where I (A), t (s), ΔV(V) and M (g) are the discharge current, discharge time, cell voltage and total mass of active materials on two electrodes, respectively.

Results and discussion

Characteristics of TMF and TMFB

The basic physical and chemical properties of TMF were shown in Table 1. The pH of TMF was close to neutral (6.8). Compared with other animal manure (Table S1†), TMF had a lower moisture content of 8.2%.[31] Besides, the bulk density of the TMF was 0.36 g cm^{-3}, and the volatile solid (VS) value of 84.45% indicated a lighter texture and higher organic content. Metal

Table 1 Characteristics of TMF

Parameter	TMF	Parameter	TMF
pH	6.86 ± 0.03	Fe (mg kg^{-1})	307.48
Moisture content (%)	8.2 ± 0.59	Hg (mg kg^{-1})	0.01
VS (%)	84.45 ± 1.16	K (mg kg^{-1})	14452.09
Density (g cm^{-3})	0.36	Mg (mg kg^{-1})	5833.16
Al (mg kg^{-1})	99.86	Mn (mg kg^{-1})	177.26
Ba (mg kg^{-1})	23.43	Na (mg kg^{-1})	124.26
Ca (mg kg^{-1})	1751.89	Ni (mg kg^{-1})	3.81
Cr (mg kg^{-1})	0.16	P (mg kg^{-1})	9701.55
Cd (mg kg^{-1})	0.02	Pb (mg kg^{-1})	0.07
Cu (mg kg^{-1})	16.24	Si (mg kg^{-1})	47.88
Zn (mg kg^{-1})	95.50		

the degree of material graphitization increases after activation and was consistent with the Raman and XRD analysis results.[39] Three peaks located at ~402.11 eV (graphitic N), ~399.67 eV (pyrrolic N), and ~397.61 eV (pyridinic N) were observed in the N 1s spectra of the four materials. After activation, the pyridinic N content increased and the graphitic N content decreased. The O 1s spectra of the four materials were all similar. Four peaks were observed at ~534.22 eV (–OH), ~533.19 eV (C–OH or C–O–O), ~531.75 eV (C–O), and ~530.79 eV (C=O).

Microscopic morphology analysis

SEM and TEM were used to study the surface morphology and porous structure of TFMB and activated TFMB samples. In Fig. 2, TMFB essentially showed the smooth surface morphology composing of closely packed carbon sheets almost without any pores. When activated at 600 degrees, the redox reaction between KOH and carbon (eqn (7)) caused the structural cleavage of TMFB from large carbon sheets to small irregular blocks with a particle size of ~10 μm. The small particles on the surface of the activated TMFB sample probably derived from metals (such as K, Ca, and Al) present in the biomass precursor.[40,41] After activation at 700 °C, the surface of TMFB-700A become rough and the unique honeycomb-shaped pits formed via KOH etching can be observed. At this time, KOH was basically reacted completely, while the generated K_2CO_3 decomposed to produce CO_2, which further activated the biochar material through physical activation (eqn (8) and (9)). Gas generation greatly contributed to the formation of the rich porous structure of TMFB-700A. When the activation temperature continued to increase to 800 °C, the potassium compounds (K_2CO_3, K_2O) were reduced by carbon to produce potassium vapor in the singlet state further etching biochar (eqn (10) and
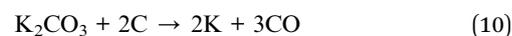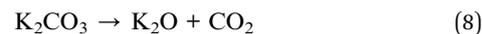
(11)). As the carbon blocks were cracked further and become smaller but thicker, the microporous structure collapsed, and the densely distributed small pits on the surface transformed into large pits. TEM observation further reveals the essential structure of carbon sheets grounded from TMFB and activated TMFB. Moreover, rough edges and abundant pores are observed in the TEM image of TMFB-700A but not in the TEM images of TMFB-600A or TMFB-800A.

$$6KOH + 2C \rightarrow 2K + 2K_2CO_3 + 3H_2 \quad (7)$$

$$K_2CO_3 \rightarrow K_2O + CO_2 \quad (8)$$

$$CO_2 + C \rightarrow 2CO \quad (9)$$

$$K_2CO_3 + 2C \rightarrow 2K + 3CO \quad (10)$$

$$K_2O + C \rightarrow 2K + CO \quad (11)$$

N$_2$ adsorption isotherms and pore size distributions

The N_2 adsorption–desorption curves and pore size distributions were shown in Fig. S3.† The four types of biochar exhibited Type-I N_2 adsorption–desorption curves.[42] The N_2 adsorption–desorption isotherm of activated TMFB rose rapidly in the $0 < P/P_0 < 0.1$ low-pressure zone, further indicating the presence of a large number of micropores. These activated micropores derived from KOH activation improved the specific surface areas of the carbon materials substantially. The N_2 adsorption–desorption isotherm in the medium-pressure zone ($0.1 < P/P_0 < 0.5$) also exhibited a significant upward trend. This indicated that the prepared carbon materials have mesopores. When the activation temperature increased to 800 °C, the TMF-800A N_2 adsorption–desorption isotherm retained a small amount of adsorption in the high-pressure zone ($0.5 < P/P_0 < 1$). This indicated that high-temperature activation made the micropores collapse to form a macroporous structure. The pore size distribution map confirmed that the number of micropores in the activated biochar sample increased significantly and that TMF-800A had significantly fewer micropores than TMF-700A after activation at 800 °C. In summary, an activation temperature of 700 °C can ensure that the TMF was fully activated, while also avoiding the harm to the specific surface area of the carbon material that was noted at higher temperatures. The surface structural characteristics of TMFB and activated TMFB were shown in Table 2. Before activation, the specific surface area of TMFB was only 232.1 m^2 g^{-1}, the micropore surface area was 222.7 m^2 g^{-1}, and the total pore volume is 0.13 cm^3 g^{-1}. After KOH activation, the surface properties of the biochar increased sharply. Upon activation at 600 °C, the specific surface area increased to 1267.9 m^2 g^{-1}, the micropore surface area increased to 1164.6 m^2 g^{-1}, and the total pore volume increased to 0.63 cm^3 g^{-1}. When activated at 700 °C, the specific surface area reached its maximum of 2081.9 m^2 g^{-1} and the total pore volume increased to 1.06 cm^3 g^{-1}. These values were almost ten times those of biochar before activation. The micropore surface
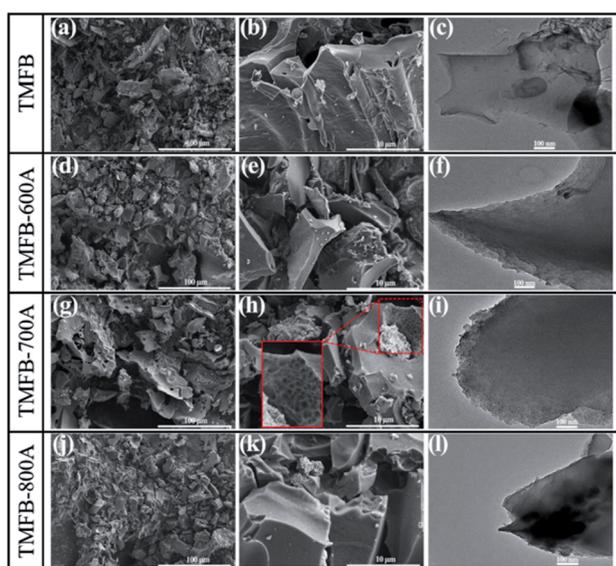

Fig. 2 SEM images: (a and b) TMFB; (d and e) TMFB-600A; (g and h) TMFB-700A; and (j and k) TMFB-800A. TEM images: (c) TMFB; (f) TMFB-600A; (i) TMFB-700A; and (l) TMFB-800A.

area increased to 1544.6 m^2 g^{-1}, which was almost seven times that before activation. After activation at 800 °C, the specific surface area decreased to 1959.3 m^2 g^{-1}. Although the total pore volume increased to 1.17 cm^3 g^{-1}, the micropore surface area decreased to 890.4 m^2 g^{-1} and the micropore volume decreased to 0.362 cm^3 g^{-1}. This further demonstrated that continuing to increase the temperature caused the microporous structure to be destroyed and became macroporous.

In Table S2,† the BET specific surface areas of TMF and TMFB-700A were compared with those of other biochar materials derived from animal manure precursors. TMF had a higher specific surface area than other unactivated animal manure biochar materials. It reached a value associated with activated forms of other animal manure biochars. It had been reported that the specific surface area of animal feces biochar was approximately 100–200 m^2 g^{-1} after activation.[31,43–46] The TMFB-700A with the highest specific surface area in this study had a surface area that was 10–20 times those of other activated animal manure biochars.[47–49]

CO$_2$ capture on TMFB

CO$_2$ capture capacity tests of TMFB and activated TMFB were performed and the experimental data were fitted by both Freundlich (Fig. 3a) and Langmuir (Fig. 3b) models.[50] The adsorption equation parameters were reported in Table S3.† Apparently, the CO$_2$ capture capacities of TMFB and activated TMFB were positively correlated with the P_{CO_2}, which was consistent with the P_{CO_2} being the thermodynamic driving force of the adsorption process. The fitted curves of both Freundlich and Langmuir models showed good agreement with the experimental adsorption isotherms of TMFB and activated TMFB, with fitted correlation coefficients (R^2) larger than 0.98. For activated TMFB, Freundlich equation seemed to be more appropriate for the entire partial pressure range, implying that heterogeneous adsorption was distributed on the biochar

surface.[51] Since the n parameter was always larger than 1, the CO$_2$ adsorption on activated TMFB was mainly physical.

The CO$_2$ capture capacities of TMF, TMFB-600A, TMFB-700A, and TMFB-800A at 0.1 MPa were 1.64, 2.09, 3.05, and 2.59 mol kg^{-1}, respectively. Among activated TMFB, TMFB-700A exhibited the best capture capacity. It can be seen from Fig. 3c that all biochars exceed 90% of their maximum capture capacities after 20 min, showing a rapid adsorption speed. TMFB-700A also exhibited the largest capture capacity in gravimetric CO$_2$ adsorption test. Its saturation value of 2.9 mol kg^{-1} at 30 min was consistent with the capture isotherm. In addition, TMFB-700A was selected for further evaluation of its CO$_2$ adsorption and desorption cycling stability (Fig. 3d). TMFB-700A maintained more than 99% of its initial capture capacity for 10 consecutive cycles, indicating that it can be regenerated easily and had excellent adsorption–desorption kinetics. Compared with the CO$_2$ capture performance of other biochar materials currently reported in Table S4,† TMFB-700A showed superior performance. The excellent CO$_2$ capture performance of TMFB-700A should be attributed to the high specific surface area and well-developed pore structure. Besides, it could also be due to the following factors: (1) O-containing (*i.e.*, carbonyl, ether, carbonyl, and hydroxyl) or N-containing (amino) functional groups on the surface of biochar produced strong electrostatic interactions with CO$_2$ molecules and provide additional adsorption sites.[52] (2) The N-containing sites (pyridine N, oxidized N, and graphitic N) not only enhanced the surface affinity between basic sites and CO$_2$ but also generated π interactions with CO$_2$.[53,54] (3) Alkali metals on the biochar surface decorated as electron donors enhanced the adsorption of CO2 as electron acceptors.[55]

Electrochemical performance

In order to explore the electrochemical performance of activated TMFB, the CV and GCD tests of three electrodes assembled from TMFB-600A, TMFB-700A, and TMFB-800A were carried out in an alkaline electrolyte. The CV curves of the three biochar materials were approximately rectangular, which was the sign of electric double-layer capacitance (EDLC) (Fig. S4a–c†). As the scanning speed increased, the TMFB-600A CV gradually deviated from rectangular but those of TMFB-700A and TMFB-800A remain rectangular. This indicated that TMFB-700A and TMFB-800A can offer good rate performance. In contrast, the pores within TMFB-600A were not as well developed as those within TMFB-700A and TMFB-800A. At high scanning speeds, the charging and discharging times were too short for ions to diffuse into the interiors of their pore networks. A pair of weak redox peaks were observed in the CV curves of the three biochar materials (~0.4 V), which were related to pseudocapacitance introduced by carboxyl groups, carbonyl groups, and metal elements.[56] As shown in Fig. S4d–f,† the GCD curves of the three biochar materials were standard triangles. This was consistent with the CV curve and also a sign of EDLC. The charge and discharge curves of TMFB-600A, TMFB-700A, and TMFB-800A all exhibited good symmetry at different current densities. This further verified that activated TMFB exhibited good capacitance behavior.
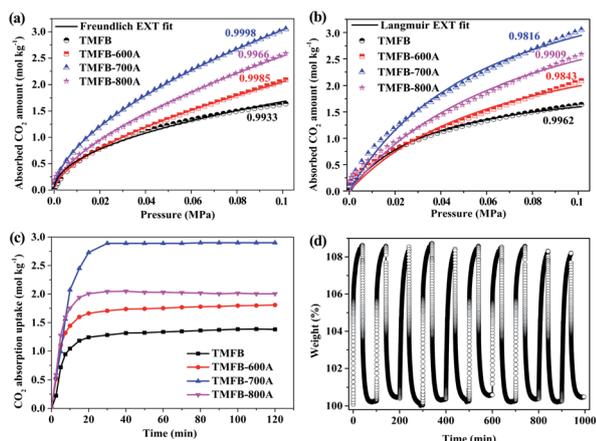

Fig. 3 Adsorption isotherms of CO$_2$ on TMFB, TMFB-600A, TMFB-700A, and TMFB-800A fitted by (a) Langmuir and (b) Freundlich models; (c) gravimetric CO$_2$ adsorption of TMFB, TMFB-600A, TMFB-700A, and TMFB-800A at 30.0 °C and 0.1 MPa; (d) gravimetric CO$_2$ uptake over 10 adsorption–desorption cycles in TGA at 30.0 °C and 0.1 MPa.

In Fig. 4a and b, the CV curves of TMFB-600A, TMFB-700A, and TMFB-800A at the same sweep speed and their GCD curves at the same current density were compared. The areas enclosed by the CV curve and the GCD curve discharge time were proportional to the specific surface areas of the three materials. This indicated that the ultra-high specific surface areas provided sufficient adsorption and desorption space for ions.[57] It also indicated that the specific surface area utilization rate of activated TMFB was quite high. The relationship between the specific capacitance calculated from the GCD curve and the current density of activated TMFB was shown in Fig. 4c. Overall, TMFB-700A offered the highest specific capacitance. This was consistent with the previous analysis and indicates that it had the best electrochemical performance. At a current density of 0.5 A g^{-1}, the reversible specific capacitances of TMFB-600A, TMFB-700A, and TMFB-800A were as high as 155.8, 335.8, and 216.2 F g^{-1}, respectively. When the current density is 10 A g^{-1}, the reversible specific capacitances of TMFB-600A, TMFB-700A and TMFB-800A were still 110.0, 273.0, and 164.0 F g^{-1}, respectively, and the capacitance retention rates were 70.6%, 81.3%, and 75.9%, respectively.

To obtain further information on the resistance of activated TMFB, electrochemical impedance spectroscopy (EIS) measurements were performed on three biochar materials at an open circuit potential in the 0.1 Hz to 100 kHz frequency range. As shown in Fig. 4d, the Nyquist diagrams of activated TMFB all included a semicircle in the low-frequency region and a diagonal line in the high-frequency region. The electrolyte resistance and the contact resistance between the active material and the nickel foam were included in the equivalent series resistance (R_s), which can be represented by the first intercept of the real axis in the high-frequency range. The diameter of the semicircle in the high-frequency region can be calculated *via* the simulation to calculate the charge transfer resistance (R_{ct}), which represented the electron transfer performance of the

material. After simulation and calculation in ZView software (Fig. S5†), the R_s values of TMFB-600A, TMFB-700A, and TMFB-800A were 0.71, 0.49, and 0.70 Ω, respectively, and the R_{ct} values were 0.02, 0.09, and 0.05 Ω, respectively. Due to the low electrical resistances of the three biochar materials, these materials had good electrical conductivity.

In practical applications, supercapacitors were assembled from two electrodes. In order to evaluate the practical application of activated TMFB in supercapacitors further, we used two TMFB-700A electrode plates of the same quality to assemble a simple TMFB-700A//TMFB-700A symmetrical capacitor. According to Fig. 5a, the TMFB-700A//TMFB-700A CV curve was approximately rectangular and consistent with the three-electrode system. Moreover, the CV curve remained perfectly rectangular at a high scanning speed of 500 mV s^{-1}. This indicated that the interface between the TMFB-700A electrode and the electrolyte can still form an electric double layer at high magnification quickly (Fig. S6†). As shown in Fig. 5b, the symmetrical capacitor assembled from TMFB-700A exhibited symmetrical charge and discharge curves. This further demonstrated that TMFB-700A//TMFB-700A had excellent electric double-layer capacitance characteristics. From the GCD curve calculation (Fig. 5c) performed with a current density of 0.5 A g^{-1}, the reversible capacitance of TMFB-700A//TMFB-700A was 244.59 F g^{-1}. Even when the current density increased by 40 times to 20 A g^{-1}, the specific capacitance of TMFB-700A//TMFB-700A was 150 F g^{-1} and the capacitance retention ratio was 80.1%. This demonstrated the excellent rate performance of the material. A comparison of the three- and two-electrode test results indicated that the specific capacitance of the three-electrode system was significantly higher than that of the
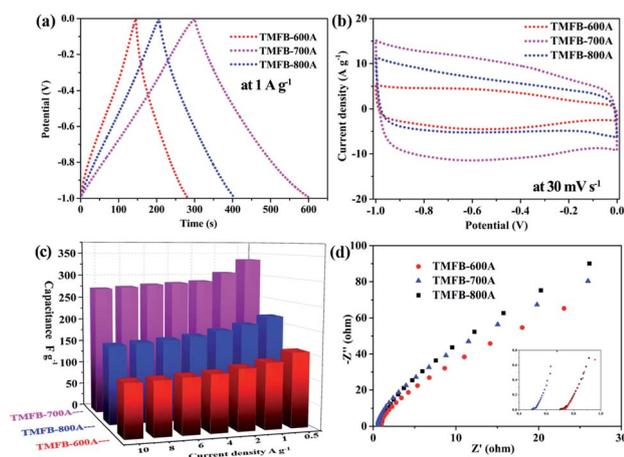
Fig. 4 (a) Comparison of the CV curves of the three biochar materials. The CV curves were measured at a scan rate of 30 mV s^{-1}. (b) Comparison of the GCD curves of three biochar materials at a current density of 1 A g^{-1}. (c) Specific capacitances of three biochar materials at various current densities. (d) Impedance Nyquist plots of three biochar materials.
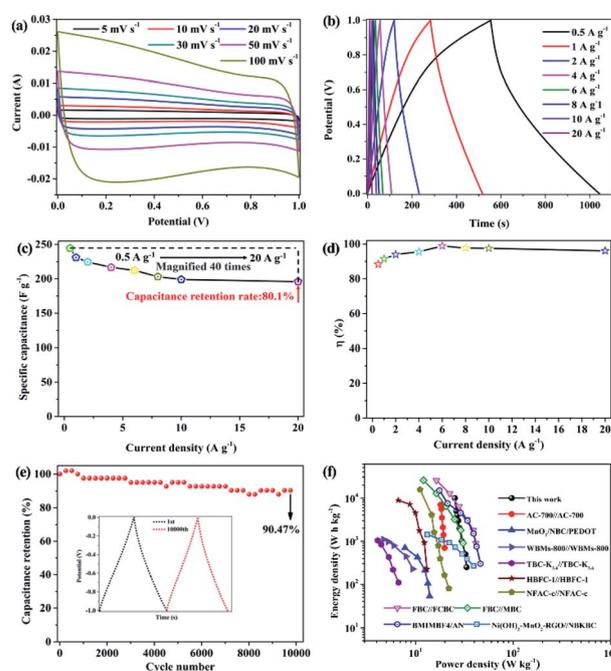
Fig. 5 The TMFB-700A//TMFB-700A (a) CV curves, (b) GCD curves, (c) specific capacitance at various current densities, (d) energy delivery efficiency, (e) cycling performance, and (f) Ragone plot.

two-electrode system. This phenomenon can be attributed to the potential window. The potential window of the two-electrode system was attributed to the two TMFB-700A electrodes. In the three-electrode system, the TMFB-700A electrode was equivalent to charging and discharging in a complete voltage range. Thus, there was a difference between the two- and three-electrode test results. The energy transfer efficiency of TMFB-700A//TMFB-700A was measured and the results are shown in Fig. 5d. The energy transmission efficiency of TMFB-700A//TMFB-700A exceeded 90% at each current density (except 88.3% at 0.5 A g^{-1}) and reached a maximum of 98.8% (at 6 A g^{-1}).

The supercapacitor cycling stability was another important electrochemical performance indicator. In order to test the cycling performance of TMFB-700A further, the assembled TMFB-700A//TMFB-700A symmetrical capacitors were charged and discharged at a large current density of 4 A g^{-1}. As shown in Fig. 5e, after 10 000 cycles of testing, the TMFB-700A//TMFB-700A cycling retention rate was 90.47%, which indicated excellent cycling stability. The Ragone diagram in Fig. 5f showed that TMFB-700A//TMFB-700A can offer excellent energy and power densities. When the power density was 0.25 kW kg^{-1}, the energy density of TMFB-700A//TMFB-700A was as high as 33.97 W h kg^{-1}. Even when the energy density was 27.22 W h kg^{-1}, the power density was as high as 10 kW kg^{-1}. When compared with other reported biochar capacitors such as AC-700//AC-700 (19.9 W h kg^{-1}, 700 W kg^{-1}),[58] MnO_2/NBC/PEDOT (7.8 W h kg^{-1}, 706.3 W kg^{-1}),[59] WBMs-800//WBMs-800 (9.4 W h kg^{-1}, 227 W kg^{-1}),[60] TBC-$K_{3.6}$//TBC-$K_{3.6}$ (6.7 W h kg^{-1}, 110 W kg^{-1}),[61] HBFC-1//HBFC-1 (13.1 W h kg^{-1}, 225 W kg^{-1}),[62] and NFAC-c//NFAC-c (22 W h kg^{-1}, 80 W kg^{-1})[63] our results were superior. Meanwhile, our results were closed to other reported capacitors based on modified biochar, including FBC//FCBC (45.1 W h kg^{-1}, 900 W kg^{-1}),[64] FBC//MBC (30.8 W h kg^{-1}, 900 W kg^{-1}),[64] $BMIMBF_4$/AN (46.38 W h kg^{-1}, 300 W kg^{-1}),[65] and $Ni(OH)_2$-MnO_2-RGO//NBKBC (39.5 W h kg^{-1}, 264 W kg^{-1})[66] (Table S5†).

The excellent electrochemical performance of TMFB-700A can be attributed to the following factors: (1) the ultra-high specific surface area provides enough adsorption–desorption space for ions; (2) the unique porous structure can accelerate the electrolyte diffusion rate so that the electrolyte can quickly penetrate into the internal structure of the electrode material; (3) the developed pores provide space for buffering of ions and electrons, which facilitates their rapid transmission; (4) abundant surface functional groups not only enhance electrolyte diffusion in the electrode but also increase the overall capacitance of the material by introducing a proper amount of pseudocapacitance; and (5) the high degree of graphitization and defect structure density endow the material with excellent conductivity.

Conclusions

Herein, we have demonstrated the successful fabrication of the novel KOH activation waste-fed *Tenebrio molitor* feces biochar, and investigated in synergistic characteristic terms of CO_2 capture and electrochemical performances. When activated at 700 °C for 1 h, the specific surface area of TMFB-700A increased significantly from 232.09 to 2081.78 m^2 g^{-1}, that was 10–20 times those of other activated animal manure biochars. In addition, well-developed pore distribution and unique honeycomb microstructure with abundant surface functional groups were formed. Due to these remarkable properties, TMFB-700A can quickly adsorb a large amount of CO_2 (3.05 mol kg^{-1}) with excellent recycling performance. TMFB-700A also exhibited promising electrochemical performance (335.8 F g^{-1} at 0.5 A g^{-1}) and was used as electrode material in a symmetrical supercapacitor. It provided a high energy density of 33.97 W h kg^{-1} at a power density of 0.25 kW kg^{-1} with 90.47% capacitance retention after 10 000 charge–discharge cycles. By comparison, the CO_2 capture and supercapacitor performance of TMFB is superior to most recently reported biochar materials and close to some modified biochar materials. After the CO_2 adsorption–desorption cycles, the internal pores of the TMFB might be further enlarged to improve the electrochemical performance. However, the combination of CO_2 capture and supercapacitor applications still warrants more research. This study proposed a clean production pathway to convert TMF into promising functional biochar and offer valuable new insights for resource utilization of TMF.

Author contributions

Saier Wang: conceptualization, methodology, formal analysis, investigation, writing–original draft. Ying Shi: conceptualization, methodology, formal analysis, investigation. Huiming Xiang: writing–review & editing. Ru Liu: methodology, formal analysis. Lianghu Su: conceptualization, validation, investigation. Longjiang Zhang: writing–review & editing. Rongting Ji: conceptualization, validation, investigation.

Conflicts of interest

There are no conflicts to declare.

Acknowledgements

Notes and references

1 IPCC, *Climate Change 2022: Mitigation of Climate Change*, 2022.

2 H. Gu, G. Song, M. Niu, S. Zhao, Y. Gao and F. Li, *Chem. Eng. J.*, 2022, **441**, 135942.

3 *World Greenhouse Gas Emissions: 2018*, World Resources Institute.

4 J. Rogelj, D. Huppmann, V. Krey, K. Riahi, L. Clarke, M. Gidden, Z. Nicholls and M. Meinshausen, *Nature*, 2019, **573**, 357–363.

5 J. Zhao, S. Deng, L. Zhao, X. Yuan, B. Wang, L. Chen and K. Wu, *J. CO2 Util.*, 2021, **52**, 101662.

6 L. S. de Almeida, E. Q. Oreste, J. V. Maciel, M. G. Heinemann and D. Dias, *Trends Environ. Anal. Chem.*, 2020, **26**, e00089.

7 P. D. Dissanayake, S. You, A. D. Igalavithana, Y. Xia, A. Bhatnagar, S. Gupta, H. W. Kua, S. Kim, J.-H. Kwon, D. C. W. Tsang and Y. S. Ok, *Renewable Sustainable Energy Rev.*, 2020, **119**, 109582.

8 S. Wang, S. Wang, X. Guo, Z. Wang, F. Mao, L. Su, H. Wu, K. Wang and Q. Zhang, *Inorg. Chem. Front.*, 2021, **8**, 4878–4886.

9 K. Wang, S. Wang, J. Liu, Y. Guo, F. Mao, H. Wu and Q. Zhang, *ACS Appl. Mater. Interfaces*, 2021, **13**, 15315–15323.

10 H. Stephanie, T. E. Mlsna and D. O. Wipf, *Desalination*, 2021, **516**, 115240.

11 S. P. Sohi, *Science*, 2012, **338**, 1034.

12 X. Li, J. Zhang, B. Liu and Z. Su, *J. Clean. Prod.*, 2021, **310**, 127428.

13 W. Xiang, X. Zhang, C. Cao, G. Quan, M. Wang, A. R. Zimmerman and B. Gao, *Bioresour. Technol.*, 2022, **355**, 127274.

14 J. Zhang, D. Huang, J. Shao, X. Zhang, S. Zhang, H. Yang and H. Chen, *Fuel Process. Technol.*, 2022, **231**, 107250.

15 Y. Cai, M. Zhu, X. Meng, J. L. Zhou, H. Zhang and X. Shen, *Bioresour. Technol.*, 2022, **351**, 126924.

16 Y. Qiao and C. Wu, *Carbon Capture Sci. Technol.*, 2022, **2**, 100018.

17 O. Norouzi, F. D. Maria and A. Dutta, *J. Energy Storage*, 2020, **29**, 101291.

18 A. D. Igalavithana, S. Mandal, N. K. Niazi, M. Vithanage, S. J. Parikh, F. N. D. Mukome, M. Rizwan, P. Oleszczuk, M. Al-Wabel, N. Bolan, D. C. W. Tsang, K.-H. Kim and Y. S. Ok, *Crit. Rev. Environ. Sci. Technol.*, 2017, **47**, 2275–2330.

19 Z. Dong, Y. Lin, H. Wu and M. Zhang, *Food Chem.*, 2021, **334**, 127475.

20 Y. Lou, Y. Li, B. Lu, Q. Liu, S.-S. Yang, B. Liu, N. Ren, W.-M. Wu and D. Xing, *J. Hazard. Mater.*, 2021, **416**, 126222.

21 J. Navarro del Hierro, A. Gutiérrez-Docio, P. Otero, G. Reglero and D. Martin, *Food Chem.*, 2020, **309**, 125742.

22 L. Yang, J. Gao, Y. Liu, G. Zhuang, X. Peng, W.-M. Wu and X. Zhuang, *Chemosphere*, 2021, **262**, 127818.

23 J. C. Sanchez-Hernandez, K. S. Ro, A. A. Szogi, S. Chang and B. Park, *J. Hazard. Mater.*, 2021, **408**, 124405.

24 T. Vanden Nest, F. Amery, L. Fryda, C. Boogaerts, J. Bilbao and B. Vandecasteele, *Sci. Total Environ.*, 2021, **750**, 141699.

25 M. Uchimiya, S. Hiradate and M. J. Antal, *ACS Sustain. Chem. Eng.*, 2015, **3**, 1642–1649.

26 S.-S. Yang, Y.-d. Chen, J.-H. Kang, T.-R. Xie, L. He, D.-F. Xing, N.-Q. Ren, S.-H. Ho and W.-M. Wu, *J. Clean. Prod.*, 2019, **227**, 33–47.

27 S.-S. Yang, Y.-d. Chen, Y. Zhang, H.-M. Zhou, X.-Y. Ji, L. He, D.-F. Xing, N.-Q. Ren, S.-H. Ho and W.-M. Wu, *Environ. Pollut.*, 2019, **252**, 1142–1153.

28 Y. Xu, Z. Yang, G. Zhang and P. Zhao, *J. Clean. Prod.*, 2020, **264**, 121645.

29 W. Liao, J. Drake and S. C. Thomas, *Sci. Total Environ.*, 2022, **813**, 152638.

30 S. Patel, A. Orlov, E. Ariyachandra and S. Peethamparan, *Chem. Eng. J.*, 2021, **420**, 130413.

31 L. Su, M. Chen, G. Zhuo, R. Ji, S. Wang, L. Zhang, M. Zhang and H. Li, *Sustainability*, 2021, 13.

32 J. Park, W.-w. Jeon and H. Choo, *Powder Technol.*, 2021, **392**, 286–295.

33 K. Li, Q. Liu, H. Cheng, M. Hu and S. Zhang, *Spectrochim. Acta, Part A*, 2021, **249**, 119286.

34 J. Park, S. S. Park and Y. S. Won, *Electrochim. Acta*, 2013, **107**, 467–472.

35 L. Dong, S. Li, Y. Jin, B. Hu and G. Sheng, *Appl. Surf. Sci.*, 2021, **567**, 150794.

36 P. A. d. S. Veiga, M. H. Cerqueira, M. G. Gonçalves, T. T. d. S. Matos, G. Pantano, J. Schultz, J. B. d. Andrade and A. S. Mangrich, *J. Environ. Manage.*, 2021, **285**, 112145.

37 H. Zhu, X. Liu, Y. Jiang, M. Zhang, D. Lin and K. Yang, *Chem. Eng. J.*, 2021, **422**, 130584.

38 W. Chen, Y. Fang, K. Li, Z. Chen, M. Xia, M. Gong, Y. Chen, H. Yang, X. Tu and H. Chen, *Appl. Energy*, 2020, **260**, 114242.

39 A. Herath, C. Reid, F. Perez, C. U. Pittman and T. E. Mlsna, *J. Environ. Manage.*, 2021, **296**, 113186.

40 M. Wądrzyk, P. Grzywacz, R. Janus and M. Michalik, *Renew. Energy*, 2021, **179**, 248–261.

41 J. Chen, D. Fang and F. Duan, *Appl. Energy*, 2018, **218**, 54–65.

42 P. Maziarka, C. Wurzer, P. J. Arauzo, A. Dieguez-Alonso, O. Mašek and F. Ronsse, *Chem. Eng. J.*, 2021, **418**, 129234.

43 K. Wang, N. Peng, X. Niu, G. Lu, Y. Zhong, X. Yu, C. Du, J. Gu, H. Zhou and J. Sun, *Waste Manag.*, 2021, **126**, 400–410.

44 K. Wang, N. Peng, G. Lu and Z. Dang, *Waste Biomass Valorization*, 2020, **11**, 613–624.

45 J. Qin, S. Qian, Q. Chen, L. Chen, L. Yan and G. Shen, *J. Hazard. Mater.*, 2019, **371**, 381–388.

46 P. Zhang, H. Sun, L. Yu and T. Sun, *J. Hazard. Mater.*, 2013, **244–245**, 217–224.

47 Z. Wang, F. Shen, D. Shen, Y. Jiang and R. Xiao, *J. Environ. Sci.*, 2017, **53**, 293–300.

48 N. Lee, S.-H. Hong, C.-G. Lee, S.-J. Park and J. Lee, *Chemosphere*, 2021, **278**, 130398.

49 M. Wang, S. Hu, Q. Wang, Y. Liang, C. Liu, H. Xu and Q. Ye, *J. Clean. Prod.*, 2021, **291**, 125221.

50 A. Proctor and J. F. Toro-Vazquez, in *Bleaching and Purifying Fats and Oils* (2nd edn), ed. G. R. List, AOCS Press, 2009, DOI: **https://doi.org/10.1016/B978-1-893997-91-2.50016-X**, pp. 209–219.

51 P. Ammendola, F. Raganati and R. Chirone, *Chem. Eng. J.*, 2017, **322**, 302–313.

52 X. Hu, Y. Luo, X. Wu, J. Niu, M. Tan, Z. Sun and W. Liu, *Mater. Today Energy*, 2022, **27**, 101010.

53 H. Chen, Y. Guo, Y. Du, X. Xu, C. Su, Z. Zeng and L. Li, *Chem. Eng. J.*, 2021, **415**, 128824.

54 L. Ma, R. Bai, G. Hu, R. Chen, X. Hu, W. Dai, H. F. M. Dacosta and M. Fan, *Energy Fuels*, 2013, **27**, 5433–5439.

55 Y.-C. Chiang and R.-S. Juang, *J. Taiwan Inst. Chem. Eng.*, 2017, **71**, 214–234.

56 K. Wang, Q. Li, Z. Ren, C. Li, Y. Chu, Z. Wang, M. Zhang, H. Wu and Q. Zhang, *Small*, 2020, **16**, 2001987.

57 K. Wang, R. Bi, M. Huang, B. Lv, H. Wang, C. Li, H. Wu and Q. Zhang, *Inorg. Chem.*, 2020, **59**, 6808–6814.

58 M. Gao, W.-K. Wang, Y.-M. Zheng, Q.-B. Zhao and H.-Q. Yu, *Chem. Eng. J.*, 2020, **402**, 126171.

59 H. R. Kim, J. H. Lee, S. K. Lee, Y. Chun, C. Park, J.-H. Jin, H. U. Lee and S. W. Kim, *J. Clean. Prod.*, 2021, **284**, 125449.

60 Y. Ma, D. Yao, H. Liang, J. Yin, Y. Xia, K. Zuo and Y.-P. Zeng, *Electrochim. Acta*, 2020, **352**, 136452.

61 S. Pérez-Rodríguez, O. Pinto, M. T. Izquierdo, C. Segura, P. S. Poon, A. Celzard, J. Matos and V. Fierro, *J. Colloid Interface Sci.*, 2021, **601**, 863–876.

62 H. A. Hamouda, S. Cui, X. Dai, L. Xiao, X. Xie, H. Peng and G. Ma, *RSC Adv.*, 2021, **11**, 354–363.

63 J. Wang, Z. Li, S. Yan, X. Yu, Y. Ma and L. Ma, *RSC Adv.*, 2019, **9**, 14797–14808.

64 S. E. M. Pourhosseini, O. Norouzi, P. Salimi and H. R. Naderi, *ACS Sustain. Chem. Eng.*, 2018, **6**, 4746–4758.

65 C. Chang, H. Wang, Y. Zhang, S. Wang, X. Liu and L. Li, *ACS Sustain. Chem. Eng.*, 2019, **7**, 10763–10772.

66 G. S. d. Reis, H. P. d. Oliveira, S. H. Larsson, M. Thyrel and E. Claudio Lima, *Nanomaterials*, 2021, **11**, 424.